# Lagrangian velocity and acceleration statistics of fluid and inertial particles measured in pipe flow with 3D Particle Tracking Velocimetry

J. L. G. Oliveira[a)1], C. W. M. van der Geld[b)2], J. G. M. Kuerten[c)2]

[1]*Mobility Department, Federal University of Santa Catarina, Joinville/SC, 89218-000, Brazil*

[2]*Department of Mechanical Engineering, Eindhoven University of Technology, P.O. Box 513, NL-5600 MB Eindhoven, The Netherlands*

Three-dimensional particle tracking velocimetry (3D-PTV) has been applied to *particle-laden* pipe flow at Reynolds number 10,300, based on the bulk velocity and the pipe diameter. The volume fraction of the inertial particles was equal to $1.4 \times 10^{-5}$. Lagrangian velocity and *acceleration* statistics were determined both for tracers and for *inertial* particles with Stokes number equal to 2.3, based on the particle relaxation time and the viscous time scale. The decay of Lagrangian velocity and acceleration correlation functions was measured both for the fluid and for the dispersed phase at various radial positions. The decay of Lagrangian velocity correlations is faster for inertial particles than for flow tracers, whereas the decay of Lagrangian acceleration correlations is about 25 % slower for inertial particles than for flow tracers. Further differences between inertial and tracer particles are found in velocity fluctuations evaluated for both positive and negative time lags. The asymmetry in time of velocity cross-correlations is more pronounced for inertial particles. Quadrant analysis revealed another difference still near the wall: ejection and sweep events are less frequent for inertial particles than for tracers.

**Keywords:** inertial particles, acceleration statistics, turbulence, 3D particle tracking velocimetry

## 1. INTRODUCTION

Turbulent dispersed two-phase flows are ubiquitous in industry and nature. For this reason, the dispersion of pollutants in an urban environment, combustion, industrial mixing, sediment transport or the fluidized catalytic cracking of carbohydrates is often studied, Poelma *et al*. (2006). Flows of this kind are characterized by particles, droplets or bubbles dispersed within a carrier phase. Many of such flows occur in pipes, *e.g.* pneumatic conveying systems and chemical reactors, Kartusinsky *et al*. (2009). The ability to predict the behavior of this kind of flow is therefore of considerable interest. However, due to the

a) Electronic mail: This research was started when J. L. G. Oliveira was at Eindhoven University of Technology, 5600 MB Eindhoven, The Netherlands

b) Also at: Mechanical Engineering Department, Federal University of Santa Catarina, Florianópolis/SC, Brazil

c) Also at: Faculty EEMCS, University of Twente, P.O. Box 217, 7500 AE Enschede, The Netherlands

d) Emails: jorge.goes@ufsc.br; ; j.g.m.kuerten@tue.nl; c.w.m.v.d.geld@tue.nl (corresponding author) – Phone: + 31 40-247 2923

complexity of these flows, available models are usually simplifications and cannot predict fluid and particle behavior for the whole range of process conditions of interest.

Therefore, stochastic models of turbulent transport are promising, Pope (1994) and Yeung (2002). Experimental determination of statistical properties of particles in a Lagrangian frame of reference is essential for the development of stochastic models. For a complete description of particle statistics it is necessary to follow particle paths with high spatial and temporal resolution, on the order of the Kolmogorov length and time scales, $\eta$ and $\tau_k$, respectively. To capture the large-scale behavior in a turbulent pipe flow, trajectories should be tracked for long times, *i.e.* multitudes of $\tau_k$. This obviously necessitates access to an experimental measurement volume with a typical length scale on the order of the bulk velocity times the typical Lagrangian correlation time, Biferale *et al*. (2008) and Brouwers (2002).

Despite the higher practical importance of inhomogeneous turbulent flows, experimental Lagrangian results in literature are mostly restricted to homogeneous turbulence. Lagrangian measurements in flow geometries with non-zero mean velocity component are scarce. The work of Suzuki and Kasagi (2000) represents one of the few exceptions. For the industrially relevant pipe flow, only the 3D-PTV results of Walpot *et al*. (2006) and Oliveira *et al*. (2013) are available, to the best of our knowledge. These were single-phase pipe flows. Veenman (2004) provided Eulerian and Lagrangian DNS computations of single-phase pipe flow at bulk Reynolds number, $Re_b$ equal to 5,300 and 10,300. Walpot *et al*. (2006) presented experimental data for $Re_b$ = 5,300 and some preliminary results at $Re_b$ = 10,300. Recently, Oliveira *et al*. (2013) presented new experimental Lagrangian results for single-phase pipe flow at $Re_b$ = 10,300 and compared these with DNS-data of Veenman (2004). *All these results were for flow tracers only*.

The present work aims at providing Lagrangian velocity and acceleration statistics of flow tracers and one class of inertial particles (with Stokes number 2.3 based on the particle relaxation time and the viscous time scale and diameter 0.8 mm), measured simultaneously and in *particle-laden* flow. To the best of our knowledge, experimental data of this kind have not been provided up to now. 3D-PTV is applied to particle-laden pipe flow in upward vertical direction at $Re_b$ = 10,300. Here, $Re_b$ is based on the bulk velocity and the pipe diameter. The mean volumetric concentration of inertial particles is equal to $1.4 \times 10^{-5}$. The mass density of the inertial particles ($\rho_p \approx 1050$ kg/m$^3$) exceeds the mass density of the carrier fluid ($\rho_f \approx 1000$ kg/m$^3$).

The structure of the paper is as follows. In Section 2, the experimental set-up is presented, including specifications of flow tracers and inertial particles. Section 3 gives the 3D-PTV results for the particle-laden flow, in particular velocity and acceleration fluctuations of fluid and dispersed phase, velocity fluctuations for "negative" time lags and quadrant analysis. A discussion of the experimental findings is given in Section 4. Finally, conclusions are presented in Section 5.

## 2. EXPERIMENTAL SETUP

### 2.1. Test rig

Turbulent particle-laden pipe flow has been created in a water loop driven by a centrifugal pump (see Fig. 1). The in-line 3 kW centrifugal pump of type DPV18-30, manufactured by Duijvelaar pompen, allows Reynolds numbers based on the bulk velocity, $U_b$, and pipe diameter, $D$, in the range $10^3$ to $10^5$. A frequency controller permits fine-tuning of the Reynolds number by adjusting the mass flow rate of the upward vertical flow in the measurement section.

The mass flow rate is measured by means of a Micro Motion Elite CMF300 mass flow and mass density meter, whose inaccuracy is less than 0.5% of the registered flow rate. A water reservoir contains about 2 $m^3$ of water. This large amount facilitates water temperature stabilization and Reynolds number control. The temperature during a test-run was essentially constant, varying by typically 0.1ºC only. Submerged pumps are placed in the reservoir tank in order to promote homogeneous dispersion of the added tracers and inertial particles. The measurement section consists of a glass pipe to ensure optical accessibility. A water-filled rectangular glass box around the pipe minimizes optical distortions. The pipe diameter is chosen relatively large, 100 mm inner diameter, because measurements at high Reynolds numbers are required. For a certain Reynolds number, bulk velocities are lower for higher pipe diameters, which is advantageous for the acquisition of Lagrangian statistics.

A flow straightener, tube bundle conditioner of ISO 5167-1:1991 (see Miller (1996)), has been placed downstream of the 90º bend, about 45 pipe diameters upstream of the measuring section. The flow straightener removes secondary flows and shortens the length required to obtain a fully developed flow. At the location of the test section a fully developed flow has been achieved; see Oliveira *et al*. (2013).

**Fig. 1.**

### 2.2. Properties of applied particles

Properties of polystyrene particles applied in the present particle-laden flow are given in Table 1. The fluid time-scale $\tau_f$ used in the Stokes number, *St*, is based on the kinematic viscosity, $\nu$, and the wall shear velocity: $\tau_f = \nu/u_\tau^2$. For $Re_b < 10^5$, the wall shear velocity is estimated as

$$u_\tau = \left( \frac{U_b{}^2 f}{8} \right)^{0.5} \tag{1}$$

with $f = a\ Re_b^{-m}$, $m = 0.25$ and $a = 0.316$; see Hinze (1975), $\tau_f$ is roughly 28 ms. See also the caption of Table 1. The fluid length-scale is the Kolmogorov scale for fully developed single-phase pipe flow at $Re_b$ = 10,300 as computed by Veenman (2004). The Kolmogorov length is about 0.60 mm in the pipe core and 0.23 mm close to the wall. For evaluation of the particle timescale, $\tau_p$, the relaxation time for particles in stationary flow is used, see Albrecht *et al*. (2003):

$$\tau_p = \left( \frac{d_p{}^2 \rho_p}{18\mu} \right) \left( 1 + \frac{0.5\rho_f}{\rho_p} \right) \tag{2}$$

where $\mu$ is the dynamic viscosity, $d_p$ is the particle diameter and $\rho_p$ and $\rho_f$ are the mass densities of particles and fluid, respectively. A relaxation time of $\tau_p \approx 4$ ms is obtained for the tracers. Note that the fluid inertia is accounted for by the added mass coefficient 0.5 which close to a wall increases to about 0.7; see van der Geld (2002).

**Table 1.**

The terminal velocity specified in Table 1 is attained in a quiescent fluid when gravitational and drag forces are in equilibrium:

$$U_{TV} = \left[ \frac{4\left(\rho_p - \rho_f\right) d_p g}{3 C_D \rho_f} \right]^{0.5} \tag{3}$$

where $g$ is the gravitational acceleration and $C_D$ the drag coefficient. The latter is a function of the particle Reynolds number, $Re_p = d_p|U_{TV}|/\nu$, which is based on the particle diameter and the terminal velocity. In the Stokes regime, $C_D$ is given by Eq. (4). For For $1 < Re_p < 1000$, Schiller and Naumann (1935) proposed a correlation for $C_D$ given by Eq. (5):

$$C_D = \left( \frac{24}{\mathrm{Re}_p} \right); \mathrm{Re}_p < 1 \tag{4}$$

$$C_D = \left(\frac{24}{\mathrm{Re}_p}\right)\left(1+\frac{1}{6}\mathrm{Re}_p^{\,2/3}\right); 1 < \mathrm{Re}_p < 1000 \quad (5)$$

A value for $U_{TV}$ is obtained by an iterative computation using Eq. (3) and Eqs. (4) or (5). Since the bulk flow velocity, $U_b$, is approximately 100 mm/s, the ratio $U_b/U_{TV}$ is on the order of $10^2$ for tracer particles, see Table 1. Since $U_b >> U_{TV}$, $\tau_p<\tau_f$ and $d_p<\eta$, the employed particles work well as flow tracers. For inertial particles, the ratio $U_b/U_{TV}$ is on the order of 10, $\tau_p>\tau_f$ and $d_p>\eta$. Therefore, inertial particles have significant inertial characteristics and do not behave as tracers.

2.3. Particle tracking algorithm

A commercial 3D-PVT imaging code from La Vision GmbH, named Davis, has been used to obtain trajectories of tracers and inertial particles. Algorithmic details of the Davis PTV tracking code can be found in Maas (1996) and Dracos (1996).

The 3D-PTV procedure for identification of individual particle trajectories is given by Oliveira *et al*. (2013) and Oliveira (2012). Calibration and flow measurement images are processed in order to transfer files which contain time reference and spatial positions of individual particle trajectories to the analysis method. A maximum triangulation error of the order of 40 μm is allowed in the particle detection algorithm. Here, the necessary difference from the 3D-PTV procedure as applied by Oliveira *et al*. (2013) is the use of built-in imaging filters of Davis in order to obtain images with only inertial particles and images with only flow tracers; see Fig. 2. This task is facilitated by the bigger imaging projection area of inertial particles on the camera sensor, exceeding the projection of tracers by a factor of 16.

**Fig. 2.**

Reduced levels of noise are obtained for the trajectories of inertial particles. For tracers, noise is significant and removed in the trajectory analysis method; see Oliveira *et al*. (2013). After the imaging segmentation stage, the procedure to determine the 3D particle position and to identify particle trajectories is the same.

At the present measurements, a maximum triangulation error equal to 0.2 pixel, roughly 20 μm, was enough to identify the 3D position of particles in the measurement space; see Oliveira (2012). However, a maximum triangulation error of 0.4 pixel was established to capture longer particle trajectories which are extended to regions where the experimental uncertainties are higher. This was applied to achieve longer

time spans in Lagrangian correlation functions. A further increase of the maximum triangulation error is risky, since higher levels of measurement noise and spurious vectors can lower the quality of Lagrangian trajectories.

To remove spurious trajectories, the procedure as adopted by Oliveira *et al*. (2013) was followed. The removal of unrealistic trajectories has been accomplished by two filters: a length filter and a displacement outlier-check ($\pm 5\sigma_{r,\theta,z}$). Here, $\sigma$ represents the standard deviation of a velocity component at a specific radial position. It can be determined from results of the present data or from literature results. The length filter consists of eliminating all trajectories of tracers outside a range of minimum and maximum positions of a particle track. Particle trajectories with just a small number of positions have higher probability of being false than trajectories with a large number of positions. A minimum number of positions is therefore required in order to take a particle trajectory into account. This procedure has been proven to remove unrealistic particle trajectories. For example, elimination of particle trajectories comprising less than 10 spatial positions has been found to be efficient. On the other hand, a particle trajectory cannot exceed a maximum number of positions along the finite test section. No difference at final results was observed if the maximum limit varied from 80 to 300 positions per particle track.

Velocities derived by straightforward interpolations of consecutive 3D positions of a particle trajectory have been proved reliable to obtain pipe flow statistics. Accelerations were then derived by means of straightforward interpolations of consecutive velocities.

## 3. RESULTS

In this section, Lagrangian velocity and acceleration statistics of particle-laden pipe flow at $Re_b$ = 10,300 and with a mean inertial particle volume fraction of $1.4 \times 10^{-5}$ are presented. The experimental analysis required for inhomogeneous turbulent pipe flow is not straightforward since particles move during the time of observation to areas with other statistical properties. Discretization in space and time is necessary in such a way that enough independent data are collected in each point. The computation of Lagrangian statistics is done separately for each of the two classes of particles; see Table 1. The experimental analysis follows closely the ones presented by Oliveira (2012) and Walpot *et al*. (2007). Let $u_\gamma$ be the standard deviation of radial velocity fluctuations and let $\Delta t$ be the inverse of the frame rate at which particle motion is measured. To determine Lagrangian statistics of particle trajectories, the analysis method gathers data in discrete radial bands: $r_i \pm \Delta r$, with $\Delta r$ satisfying $2\Delta r > | u_\gamma | \Delta t$. The particle trajectory sketched in Fig. 3 contributes to the Lagrangian correlations in band $i$ from $t_{1/50}$ to $t_{6/50}$. Each

particle position from $t_{1/50}$ to $t_{6/50}$ serves as an initial position of a new trajectory. When these additional trajectories are taken into account, the number of data available for short time correlations is increased for reasons explained elsewhere, see Oliveira (2012).

**Fig. 3.**

Lagrangian velocity auto- and cross-correlations are defined by Eq. (6):

$$\rho_{km}(\tau, r) = \langle u_k(t_0) u_m(t_0 + \tau) \rangle \tag{6}$$

while the Lagrangian acceleration correlation is given by

$$\langle a_k(t_0) a_m(t_0 + \tau) \rangle \tag{7}$$

The term $t_0$ denotes an arbitrary initial time and $\tau$ the correlation time, a variable. The symbols "*u"* and "*a"* denote the fluctuation velocity and fluctuation acceleration, respectively. The local mean values are subtracted from the actual velocities and accelerations. The subscripts *k* and *m* indicate components in a cylindrical coordinate system (*r, z, θ*) centered at the pipe axis. The calculation of the correlations given by (6) and (7) is done by averaging over all particles that are situated inside a discrete band centered at a radial position *r* at a certain time $t_0$. These correlation functions depend on the radial coordinate *r* but are independent of $t_0$.

3.1. Velocity correlations

First, velocity correlations in particle-laden pipe flow are presented and discussed. Two dimensionless radial positions are chosen to present results of Lagrangian velocity auto- and cross-correlations, as defined by Eq. (6), for both classes of particles: one midway to the pipe center, *r/R* = 0.5, and another closer to the wall, *r/R*=0.7. These radial positions are sufficient to demonstrate the main inhomogeneous turbulent features of the entire particle-laden pipe flow. Confidence intervals of 95% are considered. For a quantity which is measured *n* times, with instantaneous results $x_i$ and mean ‹*x*›, the standard error is given by:

$$\sigma_m = \left[ \sum_{i=1}^{n} \frac{\left( x_i - < x > \right)^2}{n(n-1)} \right]^{0.5} \tag{8}$$

Errors of time-averaged values of a measured quantity $x$ will be estimated with the aid of this standard error.

Figure 4a shows normalized velocity autocorrelation functions for the axial component. Normalization is done with the starting point of the correlations, the value for $\tau = 0$. Solid lines represent DNS data of Veenman (2004) at the same $Re_b$ for flow tracers in single-phase flow. Diamonds and circles represent 3D-PTV data of flow tracers (FT) and inertial particles (IP), respectively. An accuracy bandwidth is only indicated for tracers at $r/R$=0.5; other bandwidths are similarly sized. Figure 4b shows the corresponding total number of correlation samples measured.

**Fig. 4.**

Lagrangian axial velocity statistics of flow tracers are similar to the ones of a single-phase fully developed pipe flow represented by DNS until a time lag, $\tau/\tau_f$, of about 20. Here, $\tau_f$ is the fluid time-scale given by $\nu/u_\tau^2$. At other radial positions, velocity correlations of flow tracers are also similar to the ones computed by DNS, up to a dimensionless time lag of about 20. Flow tracer results are similar to the single-phase flow measurements performed by Oliveira *et al*. (2013) at the same $Re_b$. In a particle-laden flow with a mean volumetric concentration of inertial particles of $1.4 \times 10^{-5}$ and with $St = 2.3$, Lagrangian statistics of flow tracers are hardly different from those in single-phase flow.

For $\tau/\tau_f > 20$, there is a sudden increase in the velocity correlation function. This increase happens for both classes of particles and is related to a reduction in the number of correlation samples, which is shown in Figure 4b. Increasing the bandwidth $\Delta r$ from 0.5 to 1.5 mm does not improve the results for longer time lags. It just increases the amount of data for correlation time spans in the range $0 < \tau/\tau_f < 18$ without significantly changing the Lagrangian velocity results for $\tau/\tau_f > 20$. A further increase in $\Delta r$ can induce significant changes in final results due to the differences in statistical flow properties along the radial coordinate. A smaller bandwidth results in a decrease of correlation samples for time lags in the range $0 < \tau/\tau_f < 18$. The bandwidth selected is therefore considered to be optimal. The evaluation of Lagrangian velocity autocorrelations at different radial positions with various bandwidths $\Delta r$ reveals that reliable results are obtained for both flow tracers and inertial particles, if a number of correlation samples exceeding approximately $1.5 \times 10^4$ is available; see Fig. 4b. A threshold of 15,000 independent data can safely be considered as sufficient to obtain reliable Lagrangian statistics, and, vice-versa, if less than 15000 independent data are available, no trustworthy correlation is obtained. A radial bandwidth, $\Delta r$, of

0.5 mm and a camera frequency of 50 Hz suffice to obtain negligible bias for Lagrangian velocity statistics of both classes of particles at $Re_b$ = 10,300. A similar requirement for the minimum number of correlation samples was observed for single phase flow by Oliveira *et al*. (2013).

Axial velocity correlations of flow tracers decay more slowly than the correlations of inertial particles, see Fig. 4. The slower decay of correlations of flow tracers is also observed for radial, azimuthal and cross-components, as will be shown below. The faster decay in the correlations of inertial particles also holds at other radial positions. A discussion about the differences in the velocity de-correlation process of both classes of particles is provided in section 4.

Figures 5 and 6 show 3D-PTV results for normalized radial and azimuthal velocity autocorrelations, respectively, at $r/R$ = 0.5 and $r/R$ = 0.7. Normalization is done with the starting value of the correlations for $\tau$ = 0. Solid lines represent DNS data of Veenman (2004) at the same $Re_b$. Diamonds and circles represent 3D-PTV data of flow tracers (FT) and inertial particles (IP), respectively. An accuracy band, with width equal to $\pm 2\sigma_m$, is indicated only for one data set, by dashed lines; it has similar magnitude for the other 3D-PTV results shown.

**Fig. 5.**

**Fig. 6.**

At radial positions closer to the pipe center ($r/R$ = 0.5), a slower decay of autocorrelation values is observed for both classes of particles. The presence of the wall causes the velocity correlations of particles to decay faster near the wall than in the pipe core. For both particle types, the axial autocorrelations decay more slowly than the tangential and radial ones.

3D-PTV and DNS results of the only non-zero cross-correlation functions, $\rho_{rz}$ and $\rho_{zr}$, are shown for $r/R$ = 0.7 in Fig. 7. The statistical error in the 3D-PTV results is indicated by the dashed lines with size equal to $\pm 2\sigma_m$, see Eq. (8). Cross-correlations involving the tangential component are equal to zero, since this component is decoupled from the other two components. This has also been found for inertial particles.

**Fig. 7.**

It is observed (Fig. 7) that cross-correlations in which the radial velocity varies, $\rho_{zr}$, decay considerably faster than the ones in which the axial component varies, $\rho_{rz}$. For example, at the correlation time $\tau = 20\tau_f$, the ratio $\rho_{zr} / \langle u_z(0)u_r(0)\rangle$ is 0.41, for inertia particles, while the ratio $\rho_{rz} / \langle u_r(0)u_z(0)\rangle$ is 0.76. This trend is similar for inertial and tracer particles and is understood as follows.

Consider $\rho_{rz}$ first. Particles that move towards the wall usually retain their original axial velocity for a while and will most likely be found at larger values of $r/R$ with a relatively large value of $u_z$. Particles moving towards the core of the pipe have negative $u_r$ and retain their initially lower axial velocity component longer. As a consequence, the average product $\langle u_r(t_0)u_z(t_0+\tau)\rangle$ for any time lag, $\tau$, is positive. This cannot be observed from Fig. 7, of course, but has been found to be true for the measurements. In addition, a particle moving in radial direction tends to retain its original axial velocity component for a while, $u_z(t_0+\tau) \approx u_z(t_0)$, resulting in a velocity fluctuation at the new location whose absolute value can exceed those of particles that did not move in radial direction. After ensemble averaging, the product $\langle u_r(t_0)u_z(t_0+\tau)\rangle$ is therefore close to $\langle u_r(t_0)u_z(t_0)\rangle$. The situation for $\langle u_z(t_0)u_r(t_0+\tau)\rangle$ is different since $\langle u_r\rangle = 0$ everywhere. Motion in radial direction is for tracer particles entirely due to turbulence and $\rho_{rz}$ therefore de-correlates (decreases with increasing $\tau$) faster than $\rho_{zr}$. The inertial particles studied might experience a mean drift towards the center, as further investigated below, but the fluctuations of the radial velocity component around the mean drift velocity are still due to turbulence. This explains the similarity of $\rho_{zr}$ for tracers and inertial particles.

The de-correlation of $\rho_{rz}$ is faster for inertial particles than for tracers (Fig. 7). One possible explanation is that these particles have a mean radial velocity component unequal to zero, as they will be observed to possess indeed. Inertia and the mean drift to areas with higher mean axial velocity components cause the later fluctuation $u_z(t_0+\tau)$ to be less than $u_z(t_0)$, in the ensemble averaged sense of $\rho_{rz}$. This will be further detailed in the next section. A lift force connected to inertia can explain this drift, but the nature of this force is not further investigated here. The difference between the statistics of tracer and inertial particles, on the other hand, is further investigated below.

### 3.2. Velocity correlations for negative time lags

With the aim of elucidating differences in Lagrangian statistics of tracers and inertial particles in particle-laden pipe flow, correlations of the velocity fluctuations are also evaluated for negative time lags. In this section, results are compared with those for positive time lags presented above.

In the DNS computations of this paper, particles are inserted at specific radial positions at the inlet, and velocity correlations for negative time lags therefore cannot be computed. However, DNS of turbulent channel flow at a frictional Reynolds number of 180 has been performed in which flow tracers which are uniformly distributed over the whole channel have been followed, see Vreman and Kuerten (2014). This enabled the calculation of velocity correlation functions also for negative time lags. The results show trends that are in agreement with the experimental findings. In the 3D PTV experiments, the particle trajectory sketched in Fig. 3 contributes to the Lagrangian correlations in band $i$ from $t_{6/50}$ to $t_{1/50}$. Each particle position from $t_{6/50}$ to $t_{1/50}$ also serves as an initial position of a new trajectory in "negative" time.

Figure 8 shows 3D-PTV results for normalized azimuthal velocity autocorrelations at $r/R$ = 0.7. Normalization is done with the starting value of the correlations for $\tau = 0$. Solid lines represent DNS data of Veenman (2004) at the same $Re_b$ for flow tracers and positive time lags. Diamonds ($\tau > 0$) and squares ($\tau < 0$) represent 3D-PTV results for flow tracers (FT). Circles ($\tau > 0$) and triangles ($\tau < 0$) represent results for inertial particles (IP).

**Fig. 8.**

The results show that autocorrelation functions of tangential velocity fluctuations are symmetric in time for flow tracers and for inertial particles: the results for positive and negative time lag coincide within measurement error. This observation is also valid for other radial positions and for the axial and radial velocity autocorrelations for both classes of particles.

This symmetry in time is, however, not observed in the Lagrangian velocity cross-correlation $\rho_{rz}$. In Fig. 9, the cross-correlation functions $\rho_{rz}$ and $\rho_{zr}$ are shown for flow tracers for both positive and negative time lags at $r/R$ = 0.7. Similar results are obtained at other radial positions. Corresponding results for inertial particles are presented in Fig. 10. DNS data of Veenman (2004) for pipe flow are available and given for positive time lags and tracers only.

**Fig. 9.**

The asymmetry in time of $\rho_{rz}$ is a consequence of the fact that the mean axial velocity component, $\langle U_z \rangle$, is monotonically decreasing with increasing distance $r$ from the center of the pipe, as will now be

explained. Consider a particle moving towards the pipe center at three different consecutive times: - $\tau$, 0 and $\tau$, $\tau$ being a short time lag. Because of inertia the axial velocity component will be approximately preserved during time $2\tau$. Let this velocity component at time $-\tau$ be the mean velocity at that radial position, $\langle U_z(-\tau)\rangle$. Other choices will be considered later. Since the particle velocity in radial direction is taken to be negative, the particle moves to a place, labeled 0, where the mean velocity is larger. That implies that $\langle U_z(0)\rangle$ exceeds $\langle U_z(-\tau)\rangle$. Because of that change only, the fluctuation component $u_z$ changes as well: $u_z(0) \approx \langle U_z(-\tau)\rangle - \langle U_z(0)\rangle < 0$. Let it now be assumed that the radial motion of the particle continues to be towards the pipe axis in the time span $[0, \tau]$. This is probably the boldest assumption that is to be made in this line of reasoning, but an important comment will be made on this assumption later. Since $\langle U_z(\tau)\rangle > \langle U_z(0)\rangle$, $u_z(\tau) \approx \langle U_z(-\tau)\rangle - \langle U_z(\tau)\rangle < u_z(0)$. Multiplication with the negative velocity component $u_r(0)$ yields $u_z(\tau)\, u_r(0) > u_z(0)\, u_r(0) > u_z(-\tau)\, u_r(0)$. The contribution of this particle alone to the cross-correlation would yield $\rho_{rz}(\tau) > \rho_{rz}(-\tau)$. Choices of the axial fluctuation velocity component at time $-\tau$ other than zero contribute either less or more to the inequality $\rho_{rz}(\tau) > \rho_{rz}(-\tau)$, but in the ensemble-average mean the inequality is preserved. If the initial radial velocity component would have been chosen to be positive, the same inequality $\rho_{rz}(\tau) > \rho_{rz}(-\tau)$ would have been derived, since the main change in the correlation $\rho_{rz}$ in time is due to the change of the reference velocity $\langle U_z\rangle$. This explains why the correlation $\rho_{rz}$ is asymmetric in time for tracer particles.

There is practically always a certain time span starting at time zero in which the radial velocity component retains its sign. In the case of tracers this time span can be easily estimated from Fig. 5 to be about half the correlation time, which amounts to about $7\tau_f$ or 200 ms. However, inertial particles will be seen to experience a mean drift (that cannot be determined from the autocorrelation) towards the center of the pipe in upflow. This drift makes the difference $\rho_{rz}(\tau) - \rho_{rz}(-\tau)$ bigger because more particles will contribute to this difference and because of the ensemble averaging that needs to be done. This explains the even bigger asymmetry in time of $\rho_{rz}$ that is found in the experiments, see Fig. 10.

**Fig. 10.**

Also for negative time lags, the cross-correlations of inertial particles de-correlate faster than those of tracer particles (Fig. 10 vs Fig. 9). The explanation given in section 3.1, under Fig. 7, also applies here.

3.3. Acceleration autocorrelations

To the best of our knowledge, acceleration statistics in turbulent flows with nonzero mean velocity component have rarely been investigated. In this section, they are investigated for the pipe flow to highlight further differences between tracers and inertial particles.

Velocity and acceleration correlation functions are related by a kinematic relationship; see Tennekes and Lumley (1997) and the analysis of stationary homogeneous isotropic turbulence of Sawford (1991), for example. Although one can anticipate from this relationship the faster decay of acceleration correlations compared to velocity correlations, it was of course of interest to experimentally verify this for the present experiments, since it quantifies the accuracy of the experimental results.

Normalized autocorrelation functions for the axial acceleration component at $r/R$=0.5 are shown in Fig. 11. Squares and triangles represent 3D-PTV data of flow tracers (FT) and inertial particles (IP), respectively. Error-bars have about the same size as symbols and are therefore not indicated.

**Fig. 11.**

Estimations of de-correlation times can be made in the following way. The smallest fluid time-scales are characterized by dissipation and are typically $\tau_k$. The velocity correlations de-correlate in intervals associated with the largest flow structures or energy-containing eddies, with typical time scale $\tau_c$. In turbulent flows $\tau_k$ is related to $\tau_c$ by the Reynolds number: $\tau_k = \tau_c \, Re^{-1/2}$. Since turbulent pipe flows are inhomogeneous in radial direction, $\tau_k$ and $\tau_c$ are functions of the radial coordinate. However, in section 2.2 a typical value for $\tau_k$ has been given as the viscous fluid time-scale $\tau_f$, estimated to be 28 ms. For $Re_b$ = 10,300 the corresponding estimate for the large scales is $\tau_c$ =2.8 s. The decay of fluctuating acceleration correlations therefore happens in shorter time than the decay of velocity correlations.

The acceleration autocorrelation function de-correlates in a period of time a few times $\tau_k$ (Fig. 11). The de-correlation of Lagrangian acceleration for both categories of particles takes place in $\tau/\tau_f \approx$ 3 to 4 (about 0.084 to 0.112 s). Therefore, it was possible to track particles until $[\langle a(t)a(t+\tau)\rangle/\langle a(0)^2\rangle]_{zz}, \approx 0$; see Eq. (7) and Fig. 11. Similar results as shown in Fig. 11 have been obtained for axial acceleration correlations at other radial positions as well as for azimuthal and radial acceleration autocorrelations. If all acceleration components are taken into account for all radial positions, the *ratio* of the de-correlation time of inertial particles to that of flow tracers is about 1.25. The increase in the de-correlation time with

increasing particle inertia is in accordance with findings in Von Kármán and wind-tunnel turbulent flow experiments; see Volk *et al*. (2011), Qureshi *et al*. (2007) and Brown *et al*. (2009).

In a turbulent von Kármán flow, Volk *et al*. (2011) obtained a linear relationship between the decay of the acceleration correlation of particles and the particle diameter, $d_p$, if $d_p$ exceeded $5\eta$. For $d_p$ less than $5\eta$, the decay time of acceleration correlation was about 5 to 30% larger than the Kolmogorov time-scale. In the present experiment, $\eta$ is about 0.6 mm at the pipe centerline as shown in the DNS of Veenman (2004). The diameter of the applied inertial particles is 0.8 mm and $d_p/\eta$ is about 1.35 in the pipe core. The ratio of the de-correlation time of inertial particles to that of flow tracers obtained for the present experiments, 1.25, has the same order of magnitude as the results of Volk *et al*. (2011) for $d_p < 5\eta$. In the next section, the differences in velocity correlation decay between tracers and inertial particles are further discussed.

### 3.4. Quadrant analysis

In section 3 it was shown that the differences between inertial particles and flow tracers are found in both the velocity and acceleration correlation functions. In this section, a quadrant analysis of events of "Burst" or "Sweep" type will help elucidating the trends found. In particular, the occurrence frequency of quadrant events of both classes of particles will be seen to provide important information concerning the interaction of particles and flow structures.

The interactions between coherent advection motions, so-called instantaneous realizations of the Reynolds stresses, and particles are now investigated. Particle motion from or to the wall can be explained through quadrant analysis; see Wallace *et al*. (1972) and Willmarth and Lu (1972). In order to facilitate comparison with previous results from literature, the usual wall-based coordinate system, with its origin at the wall ($y = (R - r)/R$), is applied in the quadrant analysis (Fig. 13); $u_y > 0$ corresponds to motion away from the pipe wall, inward to the center of the pipe. The cross-component of the Reynolds stress is decomposed in ($u_z$, $u_y$) quadrant-planes with (0,0) as a common point, distinguishing four types of events: outward motion of high-speed fluid (quadrant I), outward motion of low-speed fluid (quadrant II or ejection), inward motion of low-speed fluid (quadrant III) and motion of high-speed fluid towards the wall (quadrant IV or sweep). Ejections and sweeps contribute to turbulence production, Marchioli and Soldati (2002).

In Fig. 12 the contribution from each quadrant to the cross-component of the Reynolds stress tensor, $\langle u_y(0)\, u_z(0)\rangle$, is presented in the radial range $0.8 < r/R < 1$, *i.e.*, close to the wall. It is noted that the results

for flows without inertial particles are practically the same, so this is an essentially single-phase flow result that lends itself for comparison with previous results in the literature.

**Fig. 12.**

The shear stress at the wall is governed by the strongly coherent flow structures generated by the quasi-streamwise vortices, *i.e.* sweeps and ejections. Close to the pipe wall, the sweeps contribute most to the Reynolds stress, whereas for the region further away from the wall the ejections are the most important contributions to the Reynolds stress. Quadrants I and III stand for outward interaction (sweep being reflected back in the outer layer) and inward interaction (ejection deflected back to the wall) events, respectively; see Kunen (1984). Their contributions are expected to be smaller than the ones by quadrants II and IV. Results in Fig. 12 resemble to a certain extent the results obtained by Brodkey *et al*. (1974).

It is now investigated whether inertial particle fluxes are dominated by the same coherent flow structures that control momentum transfer to or from the wall. In the literature claims to that effect were made, see Zonta *et al*. (2012). Instantaneous realizations from flow tracers and inertial particles are decomposed into quadrants in Fig. 13a and Fig. 13b, respectively. Instantaneous measurements of the cross-component obtained by 3D-PTV are shown in the range $0.875 < r/R < 0.925$, where each quadrant contribution is well balanced (Fig. 12). For sake of clarity, only 1 in 25 points is plotted in Fig. 13 for tracers, and 1 in 5 for inertial particles.

**Fig. 13.**

For flow tracers ($St = 0.14$), most realizations (about $10^5$) are found in quadrants II and IV, 31.9 % and 32.6 % respectively, as expected. Realizations in quadrants I and III are less frequent, 21.3% and 14.2%, in that order. For inertial particles ($St = 2.31$), the total number of realizations (about $2 \times 10^4$) is concentrated in quadrants II and III, 31.4% and 38.4%, respectively. Quadrants I (outward interaction) and IV (sweep) are found less frequently, 18.2% and 12.0%, in that order. Instantaneous velocities of inertial particles are in general lower than the mean fluid flow velocity in axial direction, $u_{z,FT}$, because of buoyancy. This is the reason why in Fig. 13b quadrants II and III are more populated than the other two quadrants. In addition, the mean radial velocity is not zero for inertial particles: $u_{y,IP} = 0.5$ mm/s. Because of this mean drift, one would expect that quadrant II is more populated than quadrant III. This appears to be the case in Fig. 13 (where only 4 % of all points is plotted), but the occurrence frequencies

summarized in Table 2 for both classes of particles show a reverse population trend: 31 % in quadrant II and 38 % in quadrant III. The drift velocity is apparently too low to affect the quadrant statistics.

Table 2. Occurrence frequency [%] for $0.075 < y < 0.125$ (or $0.875 < r/R < 0.925$)

| *Particles* | Quadrant I | Quadrant II (Ejection) | Quadrant III | Quadrant IV (Sweep) |
|---|---|---|---|---|
| Flow tracers | 21.3 | 31.9 | 14.2 | 32.6 |
| Inertial particles $[U_{y,IP} - \langle U_{y,FT} \rangle]$ $[U_{z,IP} - \langle U_{z,FT} \rangle]$ | 18.2 | 31.4 | 38.4 | 12.0 |
| Inertial particles $[U_{y,IP} - \langle U_{y,IP} \rangle]$ $[U_{z,IP} - \langle U_{z,IP} \rangle]$ | 25.1 | 30.1 | 17.1 | 27.7 |

If the mean particle velocities, $\langle U_{y,IP} \rangle$ and $\langle U_{z,IP} \rangle$, are subtracted from instantaneous particle velocities, ejection and sweep events, summarized in in Table 2, are found to be dominant again: 30.1% and 27.7%, respectively. These numbers are a bit less than those for flow tracers. Apparently, inertial particles only follow the coherent structures to a certain extent. This is in agreement with the finding in the above that Lagrangian velocity correlations decay faster for particles with $St$ = 2.31 and the interpretation that will be given in section 4.

To explain the nonzero mean radial drift of inertia particles, a lift force can be hypothesized. With the instantaneous relative axial velocity between particles and tracers, $U_{z,FT} - U_{z,IP}$, and the mean axial velocity gradient at the wall-region, $\partial \langle U_z \rangle / \partial y$, the mean vorticity, a practical form of the inertia related lift force is proportional to the product $(U_{z,FT} - U_{z,IP}) \cdot \partial \langle U_z \rangle / \partial y$. The direction of this lift force is away from the wall for particles heavier than the surrounding fluid in upward flow. It is also proportional to the mass density of the liquid and the volume of the particle. It is easily seen that a lift force of this kind would explain the mean radial drift of 0.5 mm/s towards the center of the pipe. In Lagrangian computations not the mean vorticity, but the local instantaneous value of the vorticity should enter the expression for the lift force in order to explain the ejection and sweep phenomena observed for inertial particles. Such computations are beyond the scope of the present investigation, however.

## 4. DISCUSSION

The decay of Lagrangian velocity auto and cross-correlations of inertial particles takes place in shorter times than the velocity decay of flow tracers (section 3.1). One of the reasons is the so-called

crossing trajectory effect; see Wells and Stock (1983). A particle heavier than the surrounding fluid falls in an external force field, such as gravity, from one eddy to another at a rate faster than the average eddy-decay rate. A neutrally buoyant or fluid particle will generally remain within an eddy for a longer time, but drag, lift and other force exerted by the fluid may also in the case of neutrally buoyant particles cause a more independent behavior than tracers possess e.g. Aliseda and Lasheras (2011) and Oliveira (2012). Inertial particles cannot completely follow the large fluid scales owing to their inertia (in this study, mainly from their finite size) and the acceleration of the fluid volume which is named added mass. The fluctuating velocity of a particle is coherent with the fluid as long as it remains in a characteristic large eddy structure. The diameter of a flow tracer, $d_p$, is small compared to the Kolmogorov length-scale, $\eta$, in the present pipe flow,$0.33 < d_p/\eta < 1$, and the frictional drag in the particle equation of motion is more significant than all other terms, which keeps the tracer dragged by eddies in the flow. The importance of other terms in the particle equation of motion increases with the particle diameter. Particles of intermediate size in shear flows are subject to intense lift which may result in ejection of a particle from a coherent flow structure.

The equation of motion for a spherical bubble rising at high Reynolds number in turbulent flow of a liquid was derived by Sene, Hunt and Thomas (1994). The mean rise velocity and also the axial diffusivity of spherical bubbles in isotropic turbulence were calculated analytically by Spelt and Biesheuvel (1997) for the case of turbulence of weak intensity. They showed in their analysis that the behavior of a spherical bubble rising at high Reynolds number in turbulent flow of a liquid is affected by a non-dimensional turbulence intensity, $u_{rms}/U_{TV}$, and a non-dimensional length scale $L^*$ given by $L/(\tau_p.U_{TV})$. Here, $\tau_p$ is the bubble/particle relaxation time which for particles is estimated above and for bubbles can be estimated by $U_{TV}/2g$, where $g$ is the gravitational acceleration. Length scale $L$ follows from the Eulerian energy spectrum, $E(k)$: $L={}_0\int^{\infty} E(k)dk \,/\, {}_0\int^{\infty} k.E(k)dk$. Here $k$ represents the wave vector. The experimental results obtained by Poorte and Biesheuvel (2002) on the motion of gas bubbles confirmed the applicability of this analysis. The same analysis, with obvious modifications, applies to solid spherical particles. The work of Biesheuvel and co-workers has provided solid measures to estimate the effect of fluid scales of a turbulent flow on the mean motion of spherical particles.

In the pipe flow of this study, the RMSs of the fluid velocity components are functions of the radial coordinate and are given by the starting point of Lagrangian velocity correlations, $u_{rms} = \langle \rho_{km}(0,r)^2 \rangle^{0.5}$. For $u_{rms}/U_{TV} << 1$ little interaction with vortices is expected, whereas for $u_{rms}/U_{TV} >> 1$ the turbulent motion

of particles with low inertia is governed by intense interaction with flow eddies. Notice that $U_{TV}$ in a quiescent fluid is directly related to the particle diameter, $d_p$, through Eq. (3).$U_{TV}$ decreases with decreasing $d_p$ and, therefore, the ratio $u_{rms}/U_{TV}$ will increase with decreasing $d_p$. Particles can behave as fluid particles with $u_{rms}/U_{TV} >> 1$ as long as their time- and length-scales are small enough to avoid viscous effects at the particle surface. In the particle-laden flows of the present study, the ratio $u_{rms}/U_{TV}$ is of order 1 for inertial particles and of order 10 for the flow tracers. In section 2.2 it is shown that the fluid timescale based on viscous scales and the Kolmogorov scale (as obtained by DNS) exceeds the particle timescale. This suggests that the applied flow tracers are expected to behave as fluid particles, while the inertial particles are expected to interact partially with the turbulent flow structures. As a consequence, velocity correlations of inertial particles decay faster than the velocity correlations of tracers. However, the fast decay in the velocity correlations of heavy particles in turbulent flows is only expected if the particle is able to partially interact with the flow eddies ($u_{rms}/U_{TV} \approx 1$). Particles with high inertia do not interact with turbulent structures ($u_{rms}/U_{TV} \approx 0$) and are expected to keep their velocity correlated for longer periods than those of the present study. Particles with high inertia are crossing the turbulent eddies with hardly any interaction.

In contrast with the velocity correlations, the decay of Lagrangian acceleration correlations is slower for inertial particles than for flow tracers (section 3.3). Once a particle has experienced a certain acceleration, a sweep by a large eddy for example, it takes a relatively long time before it encounters an eddy with sufficient energy to alter its acceleration again. The increase in the de-correlation period of the fluctuating acceleration with increasing particle inertia is in accordance with findings in Von Kármán and wind-tunnel turbulent flow experiments; see Calzavarini *et al*. (2009) and Voth *et al*. (2002). While the inertia of a flow tracer is small and its acceleration is quickly modified in order to follow the biggest turbulent flow structures, the inertia of a heavy particle is significant, hampering adaptation of the velocity of the particle. Thus, inertial particles cannot follow all energy-containing eddies. As a result, a once obtained acceleration is preserved for a longer time, implying that the acceleration correlations of inertial particles decay more slowly than the acceleration correlations of flow tracers.

## 5. CONCLUSIONS

3D-PTV has been applied to particle-laden pipe flow at $Re_b$ = 10,300 with mean volumetric concentration of inertial particles equal to $1.4 \times 10^{-5}$. Flow statistics of the carrier phase flows have been

found to be similar to the statistics of single-phase fully developed turbulent pipe flow. In addition, velocity and *acceleration* Lagrangian statistics have been determined for *inertial* particles with Stokes number equal to 2.3, based on the particle relaxation time and viscous time scale (1). To the best of our knowledge, no measurements of Lagrangian statistics of inertial particles in a pipe flow have been reported before.

The decay of Lagrangian velocity correlations is faster for inertial particles than for flow tracers. This finding is in agreement with the finding of the quadrant analysis, that ejection and sweep events are less frequent near the wall for inertial particles with Stokes number of 2.3 than for flow tracers. On the other hand, the decay of Lagrangian acceleration correlations is about 25% slower for inertial particles than for flow tracers, for reasons explored in the previous section. Velocity correlations for both tracers and inertial particles decay in periods of time associated with the biggest flow structures or energy-containing eddies, although velocity correlations of inertial particles de-correlate faster. Accelerations de-correlate in periods of time that are on the order of a few times the Kolmogorov time scale.

Another difference between tracers and inertial particles has been found by considering negative time lags in the correlations. Cross-correlations of the velocity fluctuations tend to be more asymmetric in time reversal for inertial particles than for tracers, for reasons explained in section 3.2.

## Acknowledgements

The authors gratefully acknowledge support of this work by Brazilian National Council of Research (CNPq) through the project call “Science without borders”, protocol number: Proc. 405700/2013-0. Special thanks to Prof. Júlio César Passos from UFSC/Brazil and Dr. Coen Baltis from Eindhoven University of Technology. The authors are indebted to Prof. Borée from ENSMA/France for his valuable comments.

## References

Albrecht, H. -E. Borys, M. Damaschke, N. and Tropea, C., 2003, Laser Doppler and phase Doppler measurement techniques. Springer-Verlag.

Aliseda ,A. and Lasheras, J. C. 2011 Preferential concentration and rise velocity reduction of bubbles immersed in a homogeneous and isotropic turbulent flow, Physics of Fluids, volume 23, 093301.

Biferale, L., Bodenschatz, E., Cencini, M., Lanotte, A. S., Ouellette, N. T., Toschi, F. and Xu, H., 2008, Lagrangian structure functions in turbulence: A quantitative comparison between experiment and direct numerical simulation. Physics of Fluids, vol. 20, 065103.

Brodkey, R. S., Wallace, J. M. and Eckelmann, H., 1974, Some properties of truncated signals in boundary shear flows. J. Fluid. Mech., 63, 209-224.

Brouwers, J. J. H., 2002, On diffusion theory in turbulence. Journal of Engineering Mathematics, 44, 277-295.

Brown, R., Warhaft, Z. and Voth, G., 2009, Acceleration statistics of neutrally buoyant spherical particles in intense turbulence. Phys. Rev. Lett., 103, 194501.

Calzavarini, E., Volk, R., Bourgoin, M., Leveque, E., Pinton, J.-F. and Toschi, F., 2009, Acceleration statistics of finite-sized particles in turbulent flow: the role of Faxén forces. J. Fluid Mech. 630, 179-189.

Dracos, T., 1996, Particle tracking in three-dimensional space, in Three-dimensional velocity and vorticity measuring an image analysis techniques. Ed. Th. Dracos, Kluwer Academic Publishers.

Hinze, J. O., 1975, Turbulence. McGraw-Hill.

Kartusinsky, A. I., Michaelides, E. E., Hussainov, M. T. and Rudi, Y, 2009, Effects of the variation of mass loading and particle density in gas–solid particle flow in pipes. Powder Technology, 193, 176-181.

Kunen, J. M. G., 1984, On the detection of coherent structures in turbulent flows. Ph.D. thesis, Technische Universiteit Delft.

Maas, H. -G., 1996, Contributions of digital photogrammetry to 3D-PTV, in "Three-dimensional velocity and vorticity measuring an image analysis techniques", Ed. Th. Dracos, Kluwer Academic Publishers.

Miller, R. W., 1996, Flow Measurement Engineering Handbook, McGraw-Hill, 3rd edition.

Marchioli, C. and Soldati, A., 2002, Mechanisms for particle transfer and segregation in a turbulent boundary layer. J. Fluid Mech., vol. 468, pp. 283-315.

Oliveira, J. L. G., 2012, 3D-PTV of particle-laden turbulent pipe flows, Ph.D. thesis, Technische Universiteit Eindhoven.

Oliveira, J. L. G., van der Geld, C. W. M. and Kuerten, J. G. M., 2013, Lagrangian and Eulerian statistics of pipe flows measured with 3D-PTV at moderate and high Reynolds numbers, Flow, Turbulence and Combustion, 91 (1), 105-137 .

Poelma, C., Westerweel, J. and Ooms, G., 2006, Turbulence statistics from optical whole-field measurements in particle-laden turbulence. Experiments in Fluids 40 (3), 347-363.

Poorte, R. E. G. and Biesheuvel, A. 2002 Experiments on the motion of gas bubbles in turbulence generated by an active grid, J. Fluid Mech., vol. 461, pp. 127-154.

Pope, S. B., 1994, Lagrangian PDF methods for turbulent flows. Annu. Rev. Fluid Mech. 26, 23-63.

Qureshi, N. M., Bourgoin, M., Baudet, C., Cartellier, A. and Gagne, Y., 2007, Turbulent transport of material particles: An experimental study of finite size effects. Phys. Rev. Lett. 99 (18), pp.184502.

Schiller, L. and Naumann, Z., 1935, A drag coefficient correlation. Z. Ver. Deutsch. Ing., 77.

Sawford, B. L. 1991 Reynolds Number Effects in Lagrangian Stochastic Models of Turbulent Dispersion. Phys. Fluids A, 3 (6), 1577–1586.

Sene, K. J., Hunt, J. C. R. and Thomas, N. H., 1994, The role of coherent structures in bubble transport by turbulent shear flows. J. Fluid Mech. 259, 219-240.

Spelt, P. D. M. and Biesheuvel, A., 1997, On the motion of gas bubbles in homogeneous isotropic turbulence", J. Fluid. Mech., 336, 221-244.

Suzuki, Y. and Kasagi, N., 2000, Turbulent air-flow measurement with the aid of 3-D particle tracking velocimetry in a curved square bend. Flow, turbulence and combustion 63, 415-442.

Tennekes, H. and Lumley, J. L. 1997 A first course in turbulence, MIT Press, Cambridge.

van der Geld, C.W.M., 2002, On the motion of a spherical bubble deforming near a plane wall, Journal of Engineering Mathematics, Volume 42, Number 2, 91-118.

Veenman, M. P. B., 2004, Statistical analysis of turbulent pipe flow: A numerical approach. Ph.D. thesis, Technische Universiteit Eindhoven.

Volk, R., Calzavarini, E., Lévêque, E., and Pinton, J.-F., 2011, Dynamics of inertial particles in a turbulent von Kármán flow", J. Fluid. Mech. 668, 223-235.

Voth, G. A., Porta, A. La, Crawford, A. M., Alexandre, J. and Bodenschatz, E., 2002, Measurement of particle accelerations in fully developed turbulence. J. Fluid. Mech. 469, 121-160.

Vreman, A.W. and Kuerten, J.G.M., 2014, Statistics of spatial derivatives of velocity and pressure in turbulent channel flow. Physics of Fluids, 26:085103.

Wallace, J. M., Eckelmann, H., Brodkey, R.S., 1972, The wall region in turbulent shear flow. J. Fluid Mech. 54, 39-48.

Walpot, R. J. E., Kuerten, J. G. M. and van der Geld, C. W. M., 2006, Experimental determination of Lagrangian velocity statistics in turbulent pipe flow. Flow, Turbulence and Combustion 76(2), 163-175.

Walpot, R. J. E., van der Geld, C. W. M. and Kuerten, J. G. M., 2007, Determination of the coefficients of Langevin models for inhomogeneous turbulent flows by three-dimensional particle tracking velocimetry and direct numerical simulation, Physics of Fluids 19, 045102.

Wells, M. R. and Stock, D. E., 1983, The effects of crossing trajectories on the dispersion of particles in a turbulent flow. J. Fluid. Mech. 136, 31-62.

Willmarth, W. W. and Lu, S. S., 1972, Structure of the Reynolds stress near the wall. J. Fluid Mech. 55, 65–92.

Yeung, P. K., 2002, Lagrangian investigations of turbulence. Annu. Rev. Fluid Mech. 34, 115-142.

Zonta, F., Marchioli, C. and Soldati, A., 2012, Modulation of turbulence in forced convection by temperature-dependent viscosity. J. Fluid Mech., vol. 697, 150-174.

**Nomenclature**

| | | | |
|---|---|---|---|
| $a$ | acceleration fluctuation | $St$ | Stokes number |
| $C_D$ | drag coefficient | $t$ | time |
| $D$ | pipe diameter | $t_0$ | arbitrary initial time |

| | | | |
|---|---|---|---|
| $d_p$ | particle diameter | $u$ | velocity fluctuation |
| $f$ | Darcy friction factor | $u_{rms}$ | root-mean-square velocity of the carrier phase |
| $g$ | gravitational acceleration | $u_\gamma$ | standard deviation of radial velocity fluctuations |
| $i$ | grid point | $u_\tau$ | wall shear velocity |
| $n$ | measurement number | $U$ | instantaneous fluid velocity |
| $r$ | radial coordinate | $U_b$ | bulk flow velocity |
| $R$ | pipe radius | $U_{TV}$ | settling velocity of a particle in an infinite, stagnant pool of water |
| $Re_b$ | Reynolds number based on the bulk velocity and the pipe diameter | $x$ | value of a measured quantity; space coordinate |
| $Re_p$ | particle Reynolds number based on the particle diameter and the terminal velocity | $z$ | Axial coordinate |
| *Greek symbols* | | | |
| $\Delta r$ | discrete radial band | $\tau_c$ | Lagrangian correlation time |
| $\Delta t$ | inverse of the camera frame rate | $\tau_f$ | fluid time-scale based on viscous scales |
| $\eta$ | Kolmogorov length-scale | $\tau_k$ | Kolmogorov time-scale |
| $\theta$ | azimuthal coordinate | $\tau_p$ | relaxation time for particles in stationary flow |
| $\mu$ | dynamic viscosity | $\sigma_m$ | standard error |
| $\rho$ | mass density | $\nu$ | kinematic viscosity |
| $\rho_{km}$ | Lagrangian velocity auto- and cross-correlations | | |
| *Subscripts* | | | |
| $b$ | bulk | | |
| $i$ | discrete radial position | IP | inertial particles |
| $f$ | fluid | $k,m$ | components in a cylindrical coordinate system ($r$, $z$, $\theta$) |
| FT | flow tracers | $p$ | particle |

**FIGURE CAPTIONS**

Fig. 1. Schematic of the 3D-PTV experimental setup for particle-laden pipe flow.

Fig. 2. Photos from the left (a,d), right (b,e) and top cameras (c,f). Figures 2a, 2b and 2c present the action of imaging filters to isolate the trajectories of inertial particles, whereas Fig.'s 2d, 2e and 2f show the action of filters to segregate the tracers only.

Fig. 3. Schematic of a particle trajectory which crosses the experimental band of grid point *i*. The circles represent particle positions tracked at a frequency of 50 Hz. The particle trajectory contributes to Lagrangian correlations at grid points *i* in the way explained in the text.

Fig. 4. Comparison of measured autocorrelation functions for the axial component at $r/R = 0.5$ and $r/R = 0.7$ with DNS data of Veenman (2004). Diamonds and circles represent 3D-PTV data of flow tracers (FT) and inertial particles (IP), respectively. Dashed lines indicate 95% accuracy bands. At $r/R = 0.5$, values of $\langle u_{FT,z}(0)\rangle$ and $\langle u_{IP,z}(0)\rangle$ are 8.1 and 9.3 mm/s, respectively. At $r/R = 0.7$, values of $\langle u_{FT,z}(0)\rangle$ and $\langle u_{IP,z}(0)\rangle$ are 9.6 and 10.1 mm/s, respectively. Figure 4b shows the number of correlation samples.

Fig. 5. Comparison of measured autocorrelation functions for the radial component at $r/R = 0.5$ and $r/R = 0.7$ with DNS data. Diamonds and circles represent 3D-PTV data of flow tracers (FT) and inertial particles (IP), respectively. Dashed lines indicate 95% accuracy bands. At $r/R = 0.5$, values of $\langle u_{FT,r}(0)\rangle$ and $\langle u_{IP,r}(0)\rangle$ are 5.2 and 5.4 mm/s, respectively. At $r/R = 0.7$, values of $\langle u_{FT,r}(0)\rangle$ and $\langle u_{IP,r}(0)\rangle$ are 5.7 and 5.8 mm/s, respectively.

Fig. 6. Comparison of measured autocorrelation functions for the tangential component at $r/R = 0.5$ and $r/R = 0.7$ with DNS data. Diamonds and circles represent 3D-PTV data of flow tracers (FT) and inertial particles (IP), respectively. Dashed lines indicate 95% accuracy bands. At $r/R = 0.5$, values of $\langle u_{FT,\theta}(0)\rangle$ and $\langle u_{IP,\theta}(0)\rangle$ are 5.2 and 5.4 mm/s, respectively. At $r/R = 0.7$, values of $\langle u_{FT,\theta}(0)\rangle$ and $\langle u_{IP,\theta}(0)\rangle$ are 5.7 and 5.8 mm/s, respectively.

Fig. 7. Comparison of measured cross-correlation functions, $\rho_{rz}$ and $\rho_{zr}$, at $r/R = 0.7$ with DNS data. Diamonds and circles represent flow tracers (FT) and inertial particles (IP), respectively. Dashed lines indicate 95% accuracy bandwidth. At $r/R = 0.7$, values of $\langle u_{FT,r}(0)u_{FT,z}(0)\rangle^{1/2}$ and $\langle u_{IP,r}(0)u_{IP,z}(0)\rangle^{1/2}$ are 4.8 and 4.5 mm/s, respectively. The starting point of cross-correlations is equal: $\rho_{rz}(0) = \rho_{zr}(0)$.

Fig. 8. Measured autocorrelation functions for the tangential component at $r/R = 0.7$ for positive and negative time lags.

Fig. 9. Measured $\rho_{rz}$ and $\rho_{zr}$ cross-correlation functions for flow tracers at $r/R = 0.7$ for positive and negative time lags. Diamonds ($\tau > 0$) and squares ($\tau < 0$) represent 3D-PTV data for $\rho_{rz}$. Circles ($\tau > 0$) and triangles ($\tau < 0$) represent data for $\rho_{zr}$.

Fig. 10. Measured $\rho_{rz}$ and $\rho_{zr}$ cross-correlation functions for inertial particles at $r/R = 0.7$ for positive and negative time lags. Diamonds ($\tau > 0$) and squares ($\tau < 0$) represent 3D-PTV data for $\rho_{rz}$. Circles ($\tau > 0$) and triangles ($\tau < 0$) represent data for $\rho_{zr}$.

Fig. 11. Normalized autocorrelation functions for the axial acceleration component at $r/R$=0.5. Squares and triangles represent 3D-PTV data of flow tracers (FT) and inertial particles (IP), respectively.

Fig. 12. Quadrant contribution to $\langle u_r(0)\ u_z(0)\rangle$ in particle-laden pipe flow. Each quadrant parcel is normalized with the local average cross-component. 3D-PTV data of flow tracers is plotted in the radial range $0.8 < r/R < 1$.

Fig. 13. Quadrant analysis for flow tracers (a) and inertial particles (b) in particle-laden pipe flow in the range $0.075 < y < 0.125$ (or $0.875 < r/R < 0.925$). Note that in both figures axial and wall-normal instantaneous velocities are subtracted by the mean flow components of the tracers, $\langle U_{z,FT}\rangle$ and $\langle U_{y,FT}\rangle$, respectively.

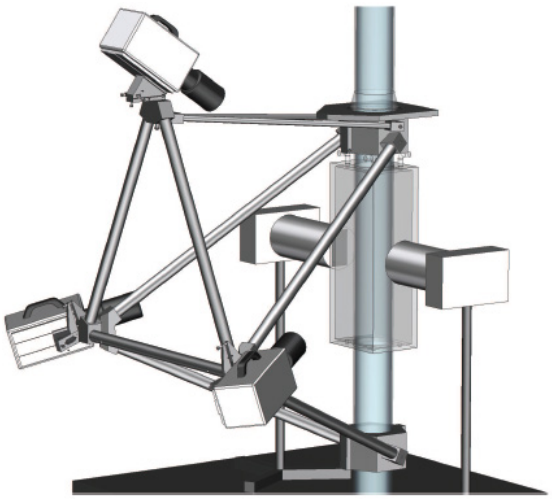

Fig. 1. Schematic of the 3D-PTV experimental setup for particle-laden pipe flow.

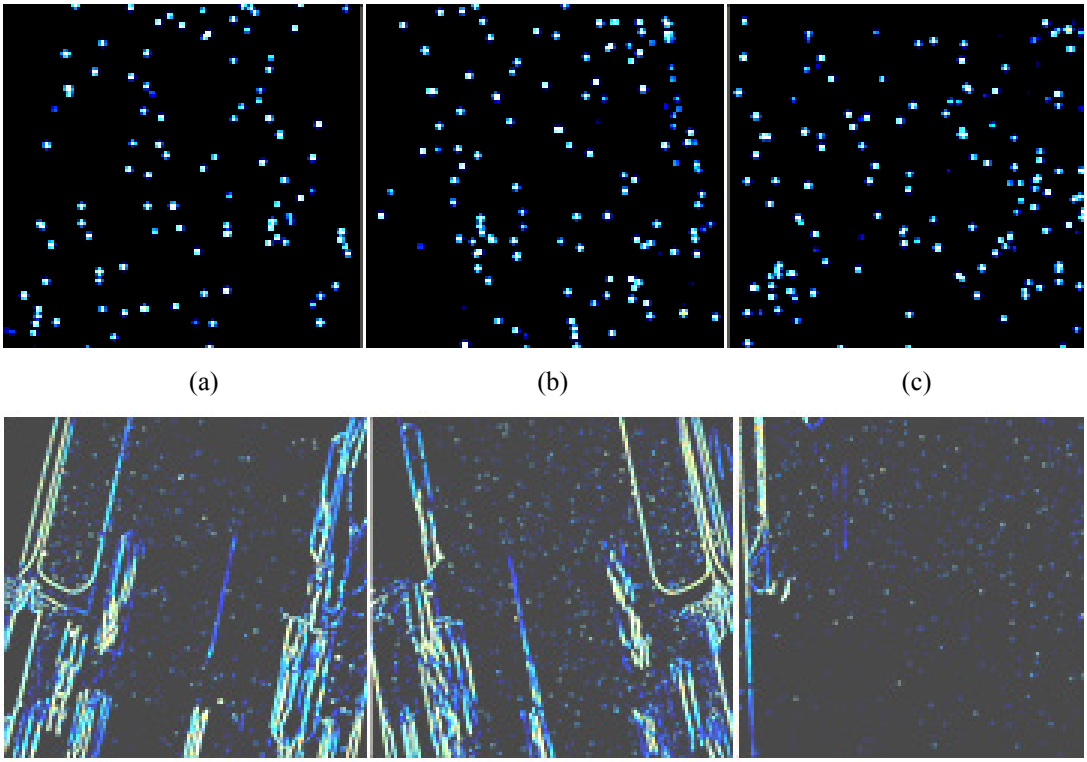

(a) (b) (c)

(d) (e) (f)

Fig. 2. Photos from the left (a,d), right (b,e) and top cameras (c,f). Figures 2a, 2b and 2c present the action of imaging filters to isolate the trajectories of inertial particles, whereas Fig.'s 2d, 2e and 2f show the action of filters to segregate the tracers only.

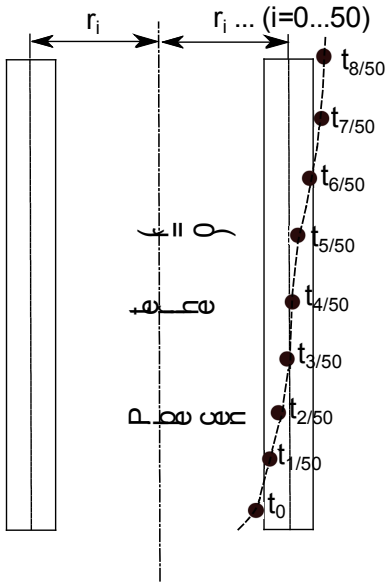


Fig. 3. Schematic of a particle trajectory which crosses the experimental band of grid point *i*. The circles represent particle positions tracked at a frequency of 50 Hz. The particle trajectory contributes to Lagrangian correlations at grid points *i* in the way explained in the text.

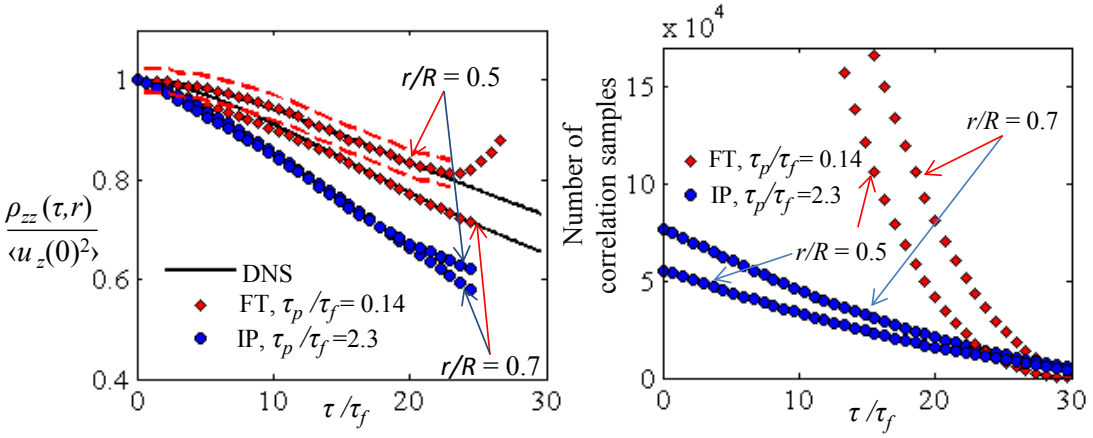


(a) (b)

Fig. 4. Comparison of measured autocorrelation functions for the axial component at $r/R$ = 0.5 and $r/R$ = 0.7 with DNS data of Veenman (2004). Diamonds and circles represent 3D-PTV data of flow tracers (FT) and inertial particles (IP), respectively. Dashed lines indicate 95% accuracy bands. At $r/R$ = 0.5, values of $\langle u_{FT,z}(0)\rangle$ and $\langle u_{IP,z}(0)\rangle$ are 8.1 and 9.3 mm/s, respectively. At $r/R$ = 0.7, values of $\langle u_{FT,z}(0)\rangle$ and $\langle u_{IP,z}(0)\rangle$ are 9.6 and 10.1 mm/s, respectively. Figure 4b shows the number of correlation samples.

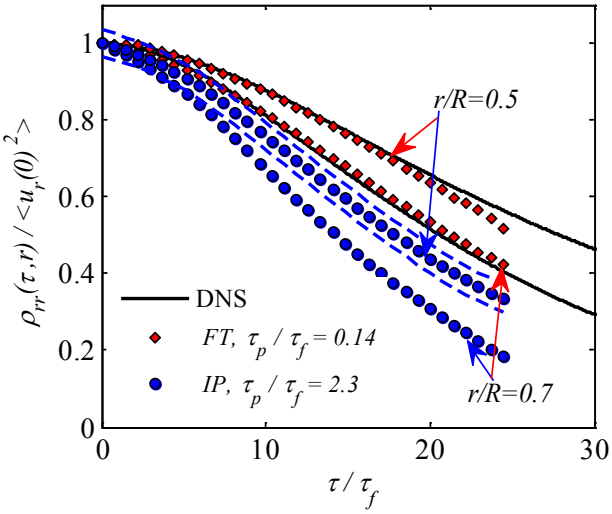


Fig. 5. Comparison of measured autocorrelation functions for the radial component at $r/R$ = 0.5 and $r/R$ = 0.7 with DNS data. Diamonds and circles represent 3D-PTV data of flow tracers (FT) and inertial particles (IP), respectively. Dashed lines indicate 95% accuracy bands. At $r/R$ = 0.5, values of $\langle u_{FT,r}(0)\rangle$ and $\langle u_{IP,r}(0)\rangle$ are 5.2 and 5.4 mm/s, respectively. At $r/R$ = 0.7, values of $\langle u_{FT,r}(0)\rangle$ and $\langle u_{IP,r}(0)\rangle$ are 5.7 and 5.8 mm/s, respectively.

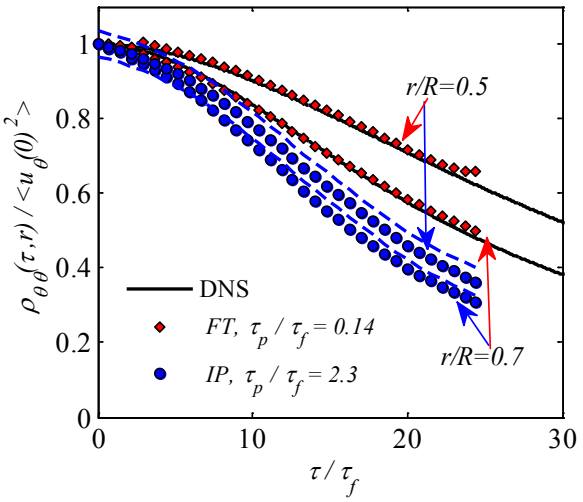


Fig. 6. Comparison of measured autocorrelation functions for the tangential component at $r/R$ = 0.5 and $r/R$ = 0.7 with DNS data. Diamonds and circles represent 3D-PTV data of flow tracers (FT) and inertial particles (IP), respectively. Dashed lines indicate 95% accuracy bands. At $r/R$ = 0.5, values of $\langle u_{\mathrm{FT},\theta}(0)\rangle$ and $\langle u_{\mathrm{IP},\theta}(0)\rangle$ are 5.2 and 5.4 mm/s, respectively. At $r/R$ = 0.7, values of $\langle u_{\mathrm{FT},\theta}(0)\rangle$ and $\langle u_{\mathrm{IP},\theta}(0)\rangle$ are 5.7 and 5.8 mm/s, respectively.

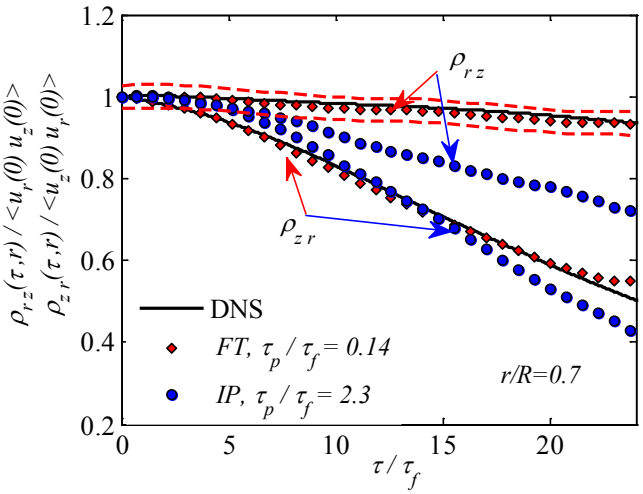


Fig. 7. Comparison of measured cross-correlation functions, $\rho_{rz}$ and $\rho_{zr}$, at $r/R = 0.7$ with DNS data. Diamonds and circles represent flow tracers (FT) and inertial particles (IP), respectively. Dashed lines indicate 95% accuracy bandwidth. At $r/R = 0.7$, values of $\langle u_{\mathrm{FT},r}(0)u_{\mathrm{FT},z}(0)\rangle^{1/2}$ and $\langle u_{\mathrm{IP},r}(0)u_{\mathrm{IP},z}(0)\rangle^{1/2}$ are 4.8 and 4.5 mm/s, respectively. The starting point of cross-correlations is equal: $\rho_{rz}(0) = \rho_{zr}(0)$.

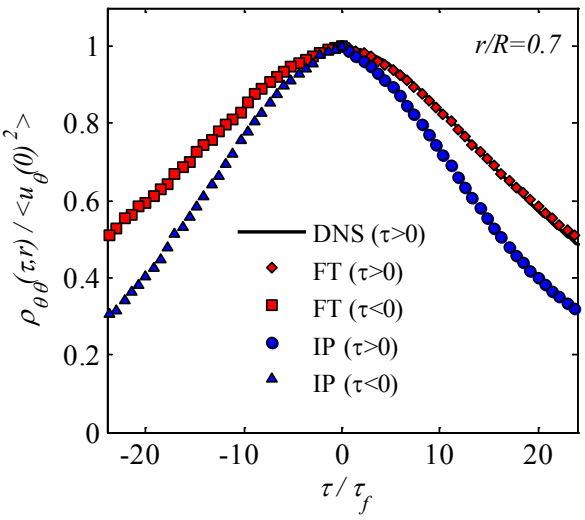


Fig. 8. Measured autocorrelation functions for the tangential component at $r/R = 0.7$ for positive and negative time lags.

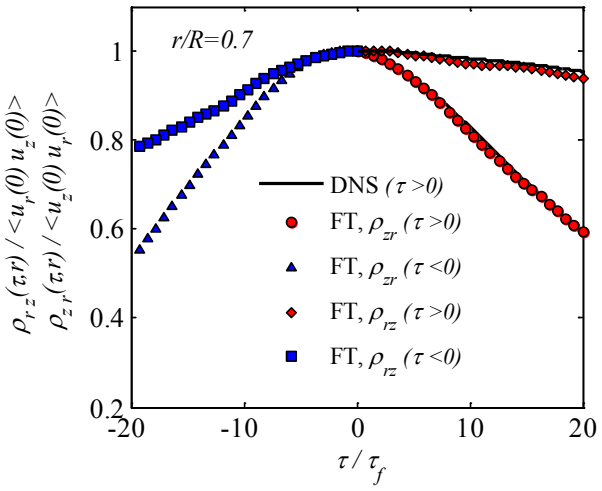


Fig. 9. Measured $\rho_{rz}$ and $\rho_{zr}$ cross-correlation functions for flow tracers at $r/R = 0.7$ for positive and negative time lags. Diamonds ($\tau > 0$) and squares ($\tau < 0$) represent 3D-PTV data for $\rho_{rz}$. Circles ($\tau > 0$) and triangles ($\tau < 0$) represent data for $\rho_{zr}$.

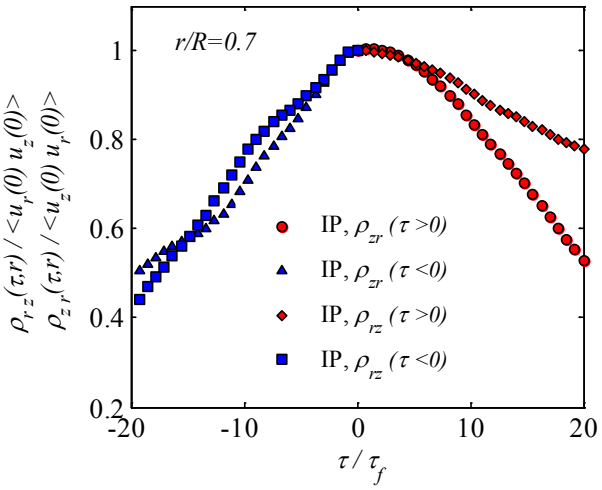


Fig. 10. Measured $\rho_{rz}$ and $\rho_{zr}$ cross-correlation functions for inertial particles at $r/R = 0.7$ for positive and negative time lags. Diamonds ($\tau > 0$) and squares ($\tau < 0$) represent 3D-PTV data for $\rho_{rz}$. Circles ($\tau > 0$) and triangles ($\tau < 0$) represent data for $\rho_{zr}$.

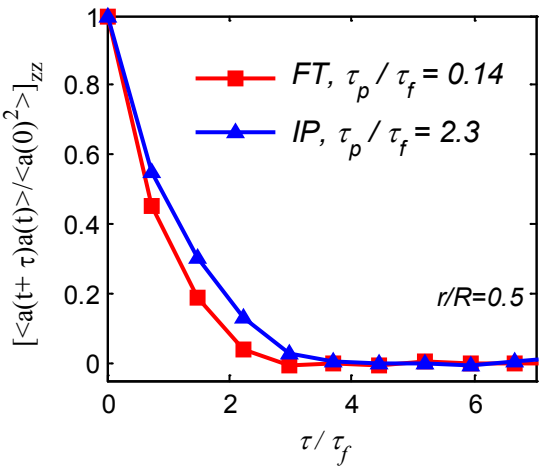


Fig. 11. Normalized autocorrelation functions for the axial acceleration component at *r/R*=0.5. Squares and triangles represent 3D-PTV data of flow tracers (FT) and inertial particles (IP), respectively.

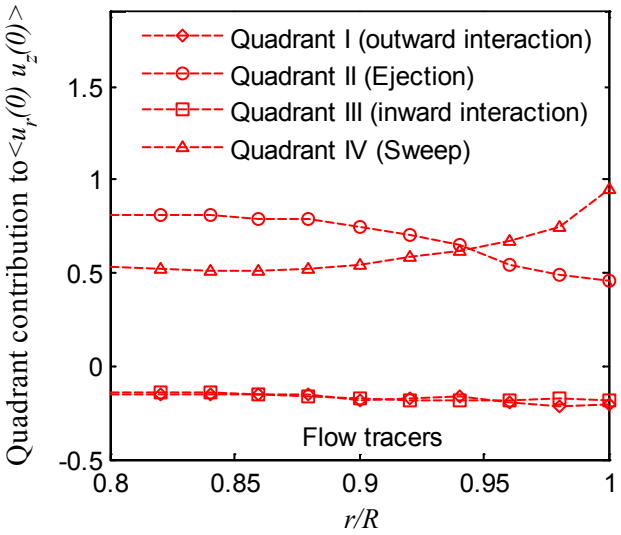


Fig. 12. Quadrant contribution to $\langle u_r(0)\ u_z(0)\rangle$ in particle-laden pipe flow. Each quadrant parcel is normalized with the local average cross-component. 3D-PTV data of flow tracers is plotted in the radial range $0.8 < r/R < 1$.

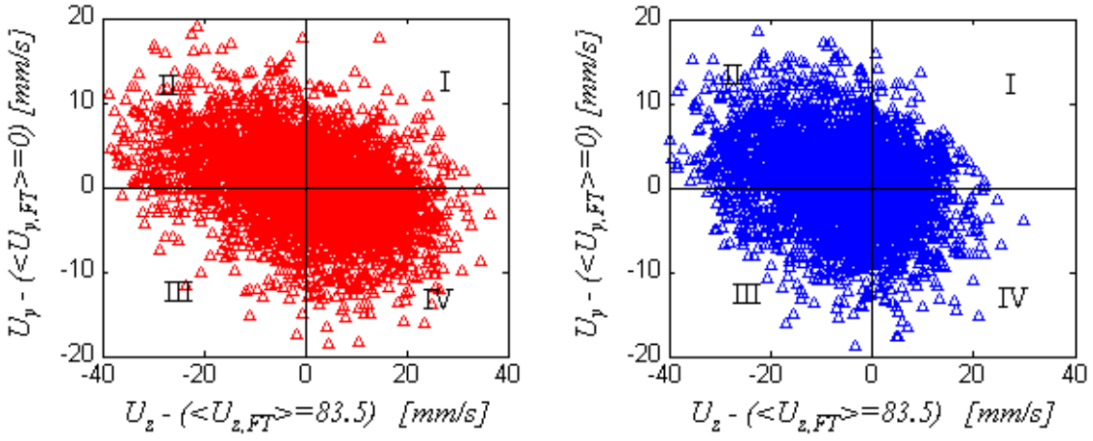


(a) (b)

Fig. 13. Quadrant analysis for flow tracers (a) and inertial particles (b) in particle-laden pipe flow in the range $0.075 < y < 0.125$ (or $0.875 < r/R < 0.925$). Note that in both figures axial and wall-normal instantaneous velocities are subtracted by the mean flow components of the tracers, $\langle U_{z,FT} \rangle$ and $\langle U_{y,FT} \rangle$, respectively.

TABLE CAPTIONS

Table 1. Properties of particles applied in the present particle-laden flow

Table 2. Occurrence frequency [%] for $0.075 < y < 0.125$ (or $0.875 < r/R < 0.925$)

Table 1. Properties of particles applied in the present particle-laden flow

| *Particles* | *Mass density* [kg/m$^3$] | *Diameter* $d_p$ [mm] | *Terminal Velocity*[a], $U_{TV}$ [mm/s] | $Re_p$ | [b]$St = \tau_p / \tau_f$ | [c]*Length-scale ratio:* $d_p/\eta$ |
|---|---|---|---|---|---|---|
| Flow tracers | 1050 | 0.2 | 1.0 | 0.18 | 0.14 | 0.33 – 1 |
| Inertial particles | 1050 | 0.8 | 10.2 | 7.76 | 2.31 | 1.33 – 3.5 |

[a]Settling velocity of a particle in an infinite, stagnant pool of water.

[b]Fluid time-scale is based on viscous scales as given by: $\tau_f = \nu/u_\tau^2$. For $Re_b < 10^5$, the wall shear velocity can be estimated as $u_\tau = (U_b^2 f/8)^{1/2}$ with $f = a\, Re_b^{-m}$, $m = 0.25$ and $a = 0.316$; $\tau_f$ is roughly 28 ms.

[c]Kolmogorov length-scales for a fully developed single-phase pipe flow at $Re_b$ = 10,300 as computed from the DNS code developed by Veenman (2004): ≈ 0.60 mm at pipe centerline and ≈ 0.23 mm close to the wall.

Table 2. Occurrence frequency [%] for $0.075 < y < 0.125$ (or $0.875 < r/R < 0.925$)

| *Particles* | Quadrant I | Quadrant II (Ejection) | Quadrant III | Quadrant IV (Sweep) |
|---|---|---|---|---|
| Flow tracers | 21.3 | 31.9 | 14.2 | 32.6 |
| Inertial particles $[U_{y,IP} - \langle U_{y,FT} \rangle]$ $[U_{z,IP} - \langle U_{z,FT} \rangle]$ | 18.2 | 31.4 | 38.4 | 12.0 |
| Inertial particles $[U_{y,IP} - \langle U_{y,IP} \rangle]$ $[U_{z,IP} - \langle U_{z,IP} \rangle]$ | 25.1 | 30.1 | 17.1 | 27.7 |